Peeling an Onion: Layer-Wise Doppler-Backprojected Ultrasound Microvascular Vector Flow Imaging

Zetao Fei[1], Chuling Ye[1], Liansheng Wang[1,2], and Yinran Chen[1,2](✉)

[1] Fujian Key Laboratory of Urban Intelligent Sensing and Computing, School of Informatics, Xiamen University, Xiamen 361005, China
[2] National Institute for Data Science in Health and Medicine, Xiamen University, Xiamen 361005, China
yinran_chen@xmu.edu.cn

Abstract. Ultrasound microvascular vector flow imaging (VFI) is essential for analyzing microvascular hemodynamics. Existing methods typically utilize angular-wise Doppler velocities combined with the least-squares (LS) optimization to estimate the vector flow field. However, the effectiveness of LS-VFI is limited due to the intrinsic instability of LS in multi-angle ultrafast beamforming. Motivated by the characteristics of microvasculature, this paper summarizes two fundamental assumptions for microvascular blood flow and proposes a novel method for microvascular vector flow imaging. Our method leverages the morphological features and angular-wise Doppler velocities to estimate the direction vector field. Then our method recovers the microvascular vector flow field by backprojecting the Doppler velocities onto the direction vector field. Particularly, the estimation of the direction vector field employs a layer-wise peeling on the microvascular networks, like peeling an onion. The backprojection is realized via a weighted global optimization. Extensive 2D and 3D experiments demonstrate that our method resolves the vector flow fields that better align with the microvascular networks compared to LS-VFI. Notably, our method achieves improvements in flow rates of approximately 3.2% to 38.4% in the Doppler phantom experiments.

Keywords: Ultrasound · Microvascular imaging · Vector flow · Doppler

1 Introduction

Imaging the microvasculature and analysing the hemodynamics is valuable for the diagnosis and therapy of various chronic and neurological diseases [19]. The technical advancements of ultrafast ultrasound beamforming [5,15], advanced clutter filtering [3,7,6], and denoising [13] have significantly facilitated high-sensitivity ultrasound microvascular imaging. In ultrasound microvascular imaging, ultrafast power Doppler imaging (uPDI) provides qualitative morphology and saturation of microvascular networks, whereas Doppler velocity estimation provides quantitative velocity components along the beam propagation direction [2,18].

The complete vector flow field of microvessels is necessary for the quantitative hemodynamics studies. Ultrasound localization microscopy (ULM) achieves super-resolution (SR) imaging by accumulating sparse microbubble signals. The flow velocities are also available by locating and tracking the microbubbles [8]. However, except for the long accumulation time, the hemodynamics of microbubbles is not equivalent to that of blood cells. Super-resolution ultrasound imaging using erythrocytes (SURE) emerges as a method for contrast-free SR and velocity imaging [1,17]. Although SURE requires shorter acquisition time than ULM, the time in an order of (dozens of) seconds is still too long for instantaneous vector flow imaging (VFI). As an alternative, least-squares (LS) VFI that combines multi-angle Doppler velocities with LS optimization has gradually become a representative strategy for normal and microvascular vector flow imaging [20,22,23]. However, LS-VFI is restricted by its intrinsic instability due to the limited transmit and receive angles (typically in $[-10°, 10°]$).

To address these challenges, this paper proposes a new method for ultrasound microvascular VFI that utilizes the morphology features of microvasculature and angular-wise Doppler velocities to resolve accurate flow vectors of microvessels. Our method is built on two fundamental assumptions that are deduced from the insights into the microvascular networks.

Assumption 1: The dominant velocity of microvascular flow is aligned with the vessel axis, and its instantaneous flow direction is consistent with the local geometric tangent of the vessel. At the microvascular scale, blood flow operates in a viscous-dominated, low-Reynolds-number laminar state. Consequently, velocity vectors are oriented along the vessel axis with a negligible radial component [16]. The streamlines remain nearly parallel to the vessel boundaries [12].

Assumption 2: Within the same microvascular branch, the flow field exhibits spatial continuity and smoothness. The dominant velocity directions of adjacent voxels can be considered nearly collinear and highly consistent. Because secondary flows induced by curvature are negligible at the microvascular scale [9,10,21], Assumption 1 holds even in curved or bifurcated regions.

The technical contributions of our method are clarified as follows: (1) Inspired by the procedure of peeling an onion, we develop a layer-wise peeling strategy on the microvascular networks that fuses the dual complementary paths of the centripetal edges and centrifugal centerlines. (2) In each layer, we introduce a Hessian-based direction estimator (HDE) to estimate the candidates of blood flow direction in each voxel. The Doppler velocities are used to correct the ambiguity and determine the correct direction vector field. (3) In the entire microvascular network, we propose a weighted global optimization framework to backproject the angular-wise Doppler velocities to the direction vector field for the recovery of microvascular vector flow field. The performance of our method is fully validated through 2D and 3D experiments.

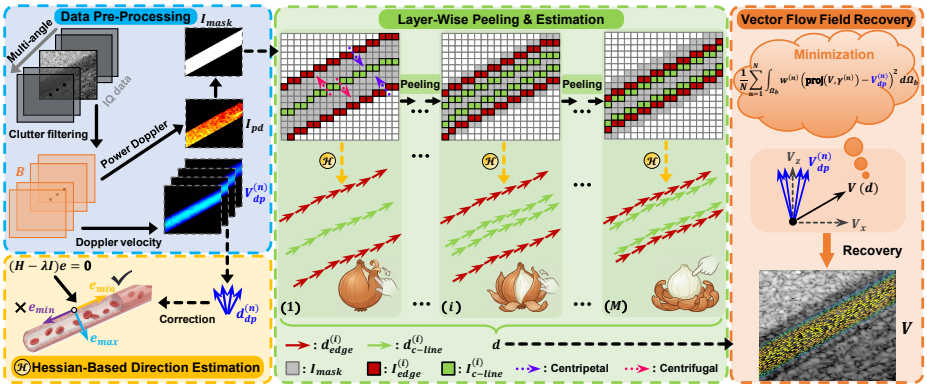

Fig. 1. Diagrams of our method for ultrasound microvascular vector flow imaging.

2 Methods

2.1 Data Pre-Processing

Our method employs an ultrafast plane-wave sequence with N steering angles and delay-and-sum (DAS) beamforming to acquire the angular-wise in-phase and quadrature-phase (IQ) beamformed data. Then, clutter filtering via singular value decomposition (SVD) is used to extract the blood flow signals $\boldsymbol{B}^{(n)} \in \mathbb{C}^{N_x,N_y,N_z,N_t}$, where $n = 1, ..., N$. $[N_x, N_y, N_z]$ and N_t are the numbers of the spatial and temporal dimensions, respectively. The angular-wise Doppler velocities are defined as:

$$\boldsymbol{v}_{dp}^{(n)} = \frac{\mathrm{PRF}c}{4\pi N f_0} \angle \{ \sum_{t=1}^{N_t-1} (\boldsymbol{B}(:,:,:,t)^{(n)} \boldsymbol{B}^*(:,:,:,t+1)^{(n)}) \}, \tag{1}$$

where PRF is the pulse repetition frequency, c is the speed of sound (1540 m/s), and f_0 is the center frequency. $\angle$ computes the angle of the complex auto-correlation coefficient. The superscript $*$ denotes conjugate.

The power Doppler image is computed as:

$$\boldsymbol{I}_{pd} = \sum_{t=1}^{N_t} |\frac{1}{N} \sum_{n=1}^{N} \boldsymbol{B}(:,:,:,t)^{(n)}|^2. \tag{2}$$

The morphology of the microvascular networks $\boldsymbol{I}_{mask} \in \{0,1\}^{N_x,N_y,N_z}$ is extracted from $\boldsymbol{I}_{pd}$ with a threshold of -15 dB. Then, $\boldsymbol{I}_{mask}$ is further refined using morphological filtering and image optimization (e.g., Gaussian smoothing) to align more closely with the underlying microvasculature.

2.2 Hessian-Based Direction Estimation

The vascular boundary of $\boldsymbol{I}_{mask}$ exhibits larger second-order derivatives in the direction perpendicular to the vessel orientation than those parallel to the ori-

entation [4]. According to this morphological property, candidates for the local blood flow direction at the boundary voxel (x, y, z) are estimated via the characteristic equation of the Hessian matrix $\boldsymbol{H}$ [11]:

$$|\lambda \boldsymbol{I} - \boldsymbol{H}| = 0, \tag{3}$$

where λ is the eigenvalue and $\boldsymbol{I}$ is the identity matrix. Solving Eq. 3 and $(\boldsymbol{H} - \lambda \boldsymbol{I})\boldsymbol{e} = 0$ yields three eigenvalues and the corresponding mutually orthogonal eigenvectors $\boldsymbol{e}$. The eigenvector $\boldsymbol{e}_{min}$ associated with the minimum eigenvalue indicates the tangential direction in the boundary voxel. According to **Assumption 1**, $\boldsymbol{e}_{min}$ serves as a candidate for the direction of blood flow.

However, $\boldsymbol{e}_{min}$ is subject to a 180-degree ambiguity, as the true blood flow is either parallel or anti-parallel to this eigenvector (see Fig. 1). To resolve this ambiguity, the angular-wise Doppler velocity direction in the voxel is utilized to correct $\boldsymbol{e}_{min}$. The direction vector of the Doppler velocity is defined as:

$$\boldsymbol{d}_{dp}^{(n)} = \text{sign}(\boldsymbol{v}_{dp}^{(n)}) \cdot \boldsymbol{d}_{tx}^{(n)}, \tag{4}$$

where $\boldsymbol{d}_{tx}^{(n)} = [\sin\theta_{tx}^{(n)} \cos\phi_{tx}^{(n)}, \sin\theta_{tx}^{(n)} \sin\phi_{tx}^{(n)}, \cos\theta_{tx}^{(n)}]$ is the unit vector indicating the direction of the transmit plane wave. θ and ϕ are the polar and azimuthal angles in the 3D coordinates, respectively. The unit direction vector $\boldsymbol{d}$ in the boundary voxel is determined as:

$$\boldsymbol{d} = \frac{1}{\|\boldsymbol{d}\|}(\text{sign}\left(\langle \boldsymbol{e}_{min}, \boldsymbol{d}_{dp}^{(n)} \rangle\right) \boldsymbol{e}_{min}), \tag{5}$$

where $\langle \cdot, \cdot \rangle$ is the inner product. In particular, the Doppler direction with the maximum absolute Doppler velocity is applied to Eqs. 4 and 5 since Eq. 4 becomes disabled when the Doppler velocity is zero, which occurs when the blood flow is perpendicular to the propagation direction of the ultrasound beam.

2.3 Layer-Wise Peeling and Estimation

Applying Section 2.2 only estimates the direction vectors of the boundary voxels. According to **Assumption 1** and **Assumption 2**, one can remove the outermost layer of the microvascular mask one-by-one and repeat HDE on the exposed layer to estimate the direction vectors in the interior of the microvessels, just like peeling an onion. Furthermore, we introduce the centerlines of the microvascular mask to assist the estimation of the direction vector field due to the following reasons. First, the centerline system inherently constitutes the skeleton of the microvasculature. It not only delineates the vessel trajectory but also defines the dominant flow trend. Second, in 2D imaging scenarios, the imaging plane cannot be precisely aligned with the longitudinal cross-sections of the microvessels due to the tortuous structure of the microvessels and considerable elevational beam widths.

According to the layer-wise peeling scheme and the assistance of the centerlines, we design two complementary paths to peel the microvascular mask: the

centripetal edge and the centrifugal centerline paths. Specifically, as illustrated in Fig. 1, the centripetal edge path iteratively peels the layers from the edges toward the centerlines, whereas the centrifugal centerline path also iteratively peels the layers in the opposite direction. The HDE operation immediately follows each peeling step to determine the direction vectors of the exposed layers. The direction vector field of the microvascular mask $\boldsymbol{d}$ is obtained after the peeling operation is completed.

2.4 Vector Flow Field Recovery

With the angular-wise Doppler velocities $\boldsymbol{v}_{dp}^{(n)}$ and the direction vector field $\boldsymbol{d}$, recovering the microvascular vector flow field remains the issue of backprojecting $\boldsymbol{v}_{dp}^{(n)}$ onto $\boldsymbol{d}$. For the n-th transmitted plane wave, the voxel-wise angle $\gamma^{(n)}$ between $\boldsymbol{v}_{dp}^{(n)}$ and $\boldsymbol{d}$ is given by:

$$\cos\gamma^{(n)} = \frac{\langle \boldsymbol{d}_{dp}^{(n)}, \boldsymbol{d} \rangle}{\|\boldsymbol{d}_{dp}^{(n)}\| \, \|\boldsymbol{d}\|}. \tag{6}$$

A straightforward way of backprojection is to directly divide $\boldsymbol{v}_{dp}^{(n)}$ by $\cos\gamma^{(n)}$ in a voxel-wise manner for the entire microvascular networks. However, this way leads to two negative consequences. First, the direct backprojection introduces the "divide-by-zero" risk when the blood flow direction is (nearly) perpendicular to the propagation direction of the ultrasound beam, i.e., $|\gamma^{(n)}| \to \pi/2$. The risk leads to locally biased estimates in the vector flow field. Second, one may wonder that the maximum absolute $\cos\gamma^{(n)}$ value could be adopted for the direct backprojection in a voxel-wise manner to mitigate the "divide-by-zero" risk. However, this strategy may deteriorate the spatial continuity of the recovered vector flow field under the low signal-to-noise ratio (SNR) condition of ultrafast ultrasound imaging.

To fully utilize the available multiple Doppler velocities in a voxel, we formulate the backprojection-based recovery of the microvascular vector flow field as a weighted global optimization problem. The optimization model seeks an optimal vector flow field, $\boldsymbol{v} = [\boldsymbol{v}_x, \boldsymbol{v}_y, \boldsymbol{v}_z] \in \mathbb{R}^{3N_b,1}$, that best fits the Doppler observations from all the N-angle plane waves in a least-squares sense. Specifically, this optimization problem aims to minimize the global discrepancy between the projected velocities and the measured Doppler velocities within the region of interest (ROI), Ω_b:

$$\boldsymbol{v} = \arg\min \frac{1}{N} \sum_{n=1}^{N} \int_{\Omega_b} w^{(n)} \left(\mathrm{proj}(\boldsymbol{v}, \gamma^{(n)}) - \boldsymbol{v}_{dp}^{(n)} \right)^2 d\Omega_b, \tag{7}$$

where $\mathrm{proj}(\cdot)$ projects the vector flow field $\boldsymbol{v}$ onto the n-th Doppler direction. The confidence weight $w^{(n)}$ is added to alleviate the numerical instability caused by near-orthogonal projections, which is defined as:

$$w^{(n)} = \frac{|\cos\gamma^{(n)}|^2}{|\cos\gamma^{(n)}|^2 + \epsilon^2}, \tag{8}$$

where $\epsilon \in (0, 0.1]$ serves as a regularization parameter. This weighting term effectively suppresses the contributions of unreliable Doppler measurements when $\cos\gamma^{(n)} \approx 0$. The exact ϵ is empirically determined within the given range based on qualitative and quantitative evaluations on the recovered vector flow field.

Note that our method is feasible for both 2D and 3D imaging scenarios. The 2D version is realized by removing the y and ϕ terms from the above derivations.

3 Experimental Configurations

The 2D experiments were conducted in a Doppler phantom with controlled flow rates of 0.39, 0.78, 1.17, and 1.67 ml/s, and an *in-vivo* liver of a healthy volunteer (male, 23 y/o). The *in-vivo* experimental protocol was approved by the anonymous committee. The imaging sequence contained four plane waves with steering angles of $[-10°, -5°, 5°, 10°]$, a center frequency of 7.5 MHz, and a PRF of 10 kHz. The sequence was implemented on an L10-5 linear array controlled by an anonymous research system.

The 3D simulations were conducted on Field II [14] by setting up a flow phantom that contains a three-cycle helical tube with a radius of 2.5 mm, a pitch of 2 mm, and an inner-tube radius of 0.5 mm. The peak velocities of the parabolic flow profiles are between 20 mm/s and 80 mm/s at a constant step of 15 mm/s. The simulated imaging sequence was a 5-angle 3D plane waves with steering angles of $0°$ and $\pm 3°$ in the $x-z$ and $y-z$ dimensions. The matrix array was designed to mimic the 8-MHz Vermon 2D probe.

We compared our method with LS-VFI [20,22,23] to evaluate its performance. The normalized root-mean-square-error (nRMSE) is used to assess the magnitudes, directions, and flow rates of the vector flow fields:

$$\text{nRMSE} = \frac{\sqrt{\frac{1}{P}\sum_{i=1}^{P}(|\boldsymbol{v}^{(i)}| - |\boldsymbol{v}_{gt}^{(i)}|)^2}}{\max(|\boldsymbol{v}_{gt}|)}, \tag{9}$$

where the subscript gt denotes ground truth. The other nRMSE is analogous to Eq. (9) with magnitude replaced with direction or flow rate.

4 Results

Fig. 2 shows the Doppler velocities, velocity magnitudes, vector flow fields, and velocity profiles of the Doppler phantom under a flow rate of 1.67 ml/s. Table 1 summarizes the quantitative evaluations. Compared to LS-VFI, the velocity magnitudes estimated by our method exhibit smoother laminar and parabolic flows. Furthermore, the flow vectors resolved by our method align more closely with the geometry of the straight tube. The quantitative measurements demonstrate that the flow rates and directions estimated by our method are closer to the ground truths. Specifically, our method improves the accuracy of flow rate estimates by around 3.2% to 38.4% when compared with LS-VFI.

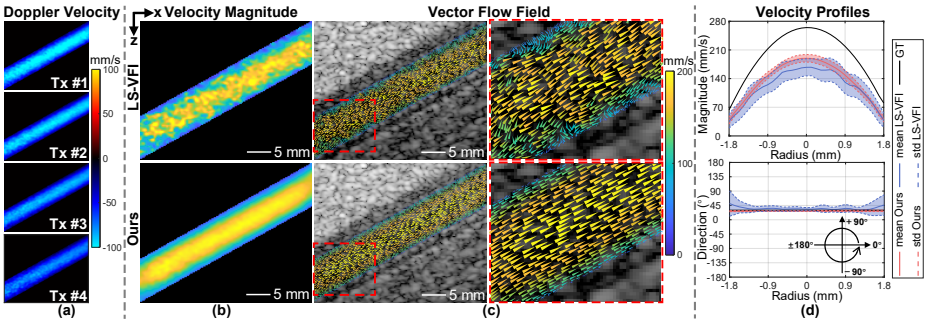

Fig. 2. Doppler velocities, velocity magnitudes, vector flow fields, and velocity profiles of the Doppler phantom under a controlled flow rate of 1.17 ml/s.

Table 1. Flow rates(ml/s), directions(30°-ground truth), and the corresponding nRMSE(%) of the Doppler phantom experiments.

Setups	0.39 ml/s		0.78 ml/s		1.17 ml/s		1.67 ml/s	
Method	LS-VFI	Ours	LS-VFI	Ours	LS-VFI	Ours	LS-VFI	Ours
Flow rate	0.24 ± 0.01	$\mathbf{0.26 \pm 0.01}$	1.12 ± 0.23	$\mathbf{0.81 \pm 0.04}$	1.38 ± 0.14	$\mathbf{1.32 \pm 0.04}$	1.60 ± 0.13	$\mathbf{1.74 \pm 0.07}$
nRMSE	37.5 ± 3.6	$\mathbf{32.8 \pm 1.9}$	44.2 ± 29.0	$\mathbf{5.8 \pm 4.0}$	16.8 ± 12.2	$\mathbf{12.7 \pm 3.5}$	8.2 ± 5.2	$\mathbf{5.0 \pm 3.1}$
Direction	32.7 ± 6.0	$\mathbf{27.2 \pm 0.7}$	22.3 ± 15.8	$\mathbf{27.2 \pm 0.7}$	35.2 ± 25.6	$\mathbf{27.2 \pm 0.7}$	35.0 ± 15.3	$\mathbf{27.2 \pm 0.7}$
nRMSE	21.1 ± 65.6	$\mathbf{9.5 \pm 1.4}$	55.6 ± 18.2	$\mathbf{9.5 \pm 1.4}$	81.8 ± 30.0	$\mathbf{9.5 \pm 1.4}$	44.8 ± 29.9	$\mathbf{9.5 \pm 1.4}$

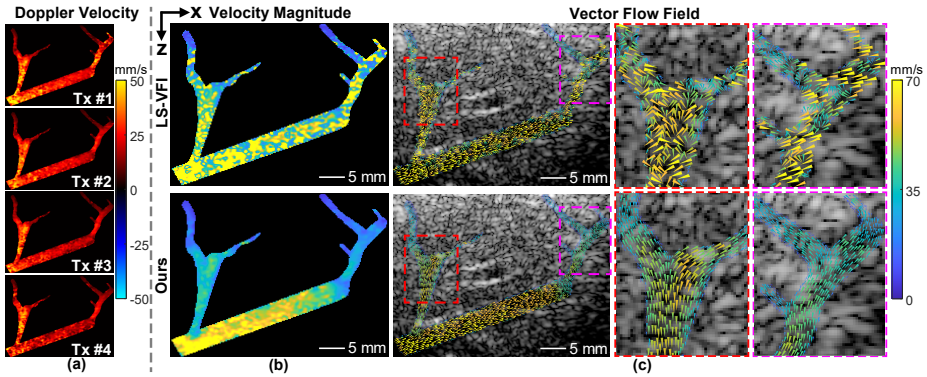

Fig. 3. Doppler velocities, velocity magnitudes, and vector flow fields of the first *in-vivo* human liver cross-section obtained by LS-VFI and ours.

Fig. 3 presents the results of the *in-vivo* human liver. The velocity magnitudes estimated by our method contain less variance than those of LS-VFI (Fig. 3(b)). Furthermore, the flow vectors of our method better align with the morphology of the underlying microvessels (Fig. 3(c)). In contrast, LS-VFI maintains less consistency between the flow vectors and the microvascular bifurcations.

Fig. 4 illustrates the vector flow fields of the 3D helical flow phantom. LS-VFI exhibits considerable variances near the edges where the velocities are low. In contrast, the flow vectors of our method align smoothly with the helical

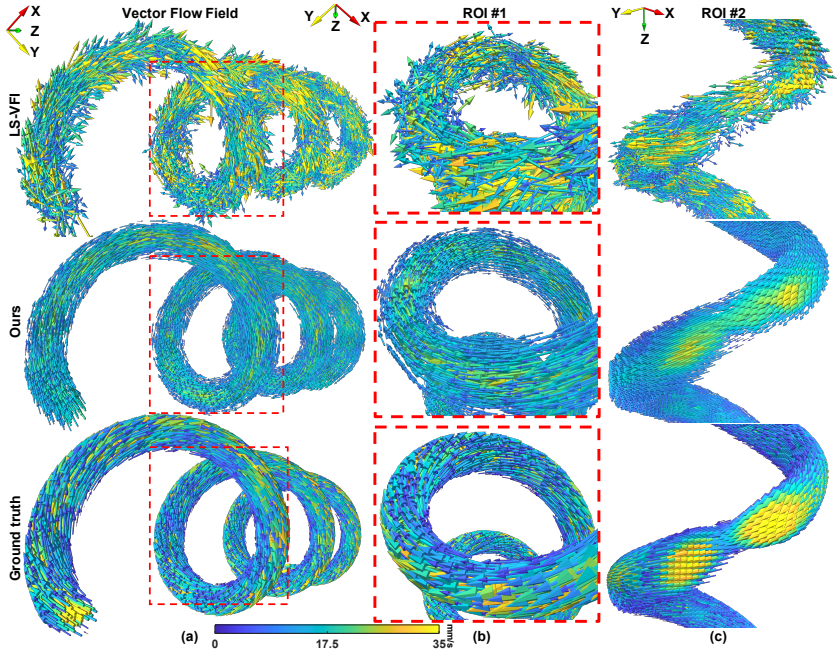

Fig. 4. Results of the 3D helical flow phantom. (a) is the overview. (b) is the zoomed-in image. (c) is the cross-sectional view that exposes the vector flow fields inside the tube.

trajectory. The cross-sectional views in Fig. 4(c) further demonstrate that our method effectively preserves the laminar and parabolic flow.

Table 2 lists the quantitative measurements in the 3D helical flow phantom. Our method reduces the nRMSE of magnitudes from $(29.25 \pm 2.3)\%$ to $(24.60 \pm 0.2)\%$, achieving an improvement of approximately 4.65%. Furthermore, the improvements are enhanced by 7.75% for the polar angle θ and by 22.45% for the azimuthal angle ϕ. Particularly, our method achieves a remarkably low nRMSE of $(0.76 \pm 0.1)\%$ in the azimuthal angle.

Table 2. nRMSE (%) of velocity magnitudes ($|v|$) and directions (θ and ϕ) in the simulations of the 3D helix flow phantom.

Setups	20 mm/s		35 mm/s		50 mm/s		65 mm/s		80 mm/s		mean ± std	
Method	LS	Ours	LS	Ours	LS	Ours	LS	Ours	LS	Ours	LS	Ours
nRMSE($\|v\|$)	32.98	**24.57**	29.77	**24.25**	28.13	**24.72**	27.18	**24.70**	28.21	**24.75**	29.25 ± 2.3	$\mathbf{24.60 \pm 0.2}$
nRMSE(θ)	16.77	**7.85**	15.61	**7.76**	15.39	**7.88**	14.44	**7.79**	15.26	**7.44**	15.49 ± 0.8	$\mathbf{7.74 \pm 0.2}$
nRMSE(ϕ)	28.34	**0.74**	24.30	**0.83**	22.28	**0.65**	19.47	**0.78**	21.42	**0.81**	23.21 ± 3.3	$\mathbf{0.76 \pm 0.1}$

5 Conclusion

This paper proposes a new method for ultrasound microvascular vector flow imaging. The method employs the morphology of microvasculature and the angular-wise Doppler velocities to estimate the direction vector field in a layer-wise manner, like peeling an onion. The recovery of the microvascular vector flow field is realized by backprojecting the Doppler velocities onto the direction vector field via a weighted global optimization. 2D and 3D experiments demonstrate the effectiveness and outperformance of our method compared to LS-VFI, showing more accurate vector flow fields that are more closely aligned with the microvasculature. Further analysis on the microvascular hemodynamics based on the resolved vector flow fields is future work.

Acknowledgments. This work was supported by the National Natural Science Foundation of China (No. 62471416), the Fujian Provincial Natural Science Foundation of China (No. 2025J09001 and 2024J01003), the Natural Science Foundation of Xiamen, China (No. 3502Z202473004), the Wang Deyao Outstanding Graduate Scholarship Program of Xiamen University, and the State Key Laboratory of Biomedical Imaging Science and System.

Disclosure of Interests. The authors have no competing interests to declare that are relevant to the content of this article.

References

1. Arendt Jensen, J., Amin Naji, M., et al.: Super-resolution ultrasound imaging using the erythrocytes—part i: Density images. IEEE Transactions on Ultrasonics, Ferroelectrics, and Frequency Control **71**(8), 925–944 (Aug 2024)
2. Aziz, M.U., Eisenbrey, J.R., Deganello, A., Zahid, M., Sharbidre, K., Robbin, M.L., et al.: Microvascular flow imaging: A state-of-the-art review of clinical use and promise. Radiology **305**(2), 250–264 (2022), pMID: 36165794
3. Baranger, J., Arnal, B., Perren, F., Baud, O., Tanter, M., Demene, C.: Adaptive spatiotemporal svd clutter filtering for ultrafast doppler imaging using similarity of spatial singular vectors. IEEE Transactions on Medical Imaging **37**(7), 1574–1586 (Jul 2018)
4. Bayat, M., Fatemi, M., Alizad, A.: Background removal and vessel filtering of non-contrast ultrasound images of microvasculature. IEEE Transactions on Biomedical Engineering **66**(3), 831–842 (Mar 2019)
5. Bercoff, J., et al.: Ultrafast compound doppler imaging: providing full blood flow characterization. IEEE Transactions on Ultrasonics, Ferroelectrics and Frequency Control **58**(1), 134–147 (Jan 2011)
6. Chen, Y., Fang, B., Li, H., Huang, L., Luo, J.: Ultrafast online clutter filtering for ultrasound microvascular imaging. IEEE Transactions on Medical Imaging **44**(6), 2477–2491 (Jun 2025)
7. Chen, Y., Fang, B., Meng, F., Luo, J., Luo, X.: Competitive swarm optimized svd clutter filtering for ultrafast power doppler imaging. IEEE Transactions on Ultrasonics, Ferroelectrics, and Frequency Control **71**(4), 459–473 (2024)

8. Dencks, S., Lowerison, M., Hansen-Shearer, J., Shin, Y., Schmitz, G., Song, P., Tang, M.X.: Super-resolution ultrasound: From data acquisition and motion correction to localization, tracking, and evaluation. IEEE Transactions on Ultrasonics, Ferroelectrics, and Frequency Control **72**(4), 408–426 (2025)
9. Ebrahimi, S., Balogh, P., Bagchi, P.: Motion of a capsule in a curved tube. Journal of Fluid Mechanics **907** (Nov 2020)
10. Feng, Z.G., Cortina, M., Chesnutt, J.K., Han, H.C.: Numerical simulation of thrombotic occlusion in tortuous arterioles. Journal of cardiology and cardiovascular medicine **2**(1), 95 (2017)
11. Frangi, A.F., Niessen, W.J., Vincken, K.L., Viergever, M.A.: Multiscale vessel enhancement filtering, p. 130–137. Springer Berlin Heidelberg (1998)
12. Goddi, A., et al.: High-frame rate vector flow imaging of the carotid bifurcation. Insights into Imaging **8**(3), 319–328 (May 2017)
13. Huang, L., et al.: Improved ultrafast power doppler imaging by using spatiotemporal non-local means filtering. IEEE Transactions on Ultrasonics, Ferroelectrics, and Frequency Control **69**(5), 1610–1624 (May 2022)
14. Jensen, J., Svendsen, N.: Calculation of pressure fields from arbitrarily shaped, apodized, and excited ultrasound transducers. IEEE Transactions on Ultrasonics, Ferroelectrics and Frequency Control **39**(2), 262–267 (Mar 1992)
15. Kou, Z., Lowerison, M.R., You, Q., Wang, Y., Song, P., Oelze, M.L.: High-resolution power doppler using null subtraction imaging. IEEE Transactions on Medical Imaging **43**(9), 3060–3071 (2024)
16. Lerendegui, M., Riemer, K., Wang, B., Dunsby, C., Tang, M.X.: Bubble flow field: a simulation framework for evaluating ultrasound localization microscopy algorithms (2022)
17. Naji, M.A., et al.: Super-resolution ultrasound imaging using the erythrocytes—part ii: Velocity images. IEEE Transactions on Ultrasonics, Ferroelectrics, and Frequency Control **71**(8), 945–959 (Aug 2024)
18. Seddiki, R., Mirault, T., Sitruk, J., Mohamedi, N., Messas, E., Goudot, G., et al.: Advancements in noncontrast ultrasound imaging for low-velocity flow: A technical review and clinical applications in vascular medicine. Ultrasound in Medicine & Biology **51**(7), 1035–1042 (2025)
19. Wardlaw, J.M., Smith, C., Dichgans, M.: Small vessel disease: mechanisms and clinical implications. The Lancet Neurology **18**(7), 684–696 (Jul 2019)
20. Yan, S., Shou, J., Yu, J., Song, J., Mao, Y., Xu, K.: Ultrafast ultrasound vector doppler for small vasculature imaging. IEEE Transactions on Ultrasonics, Ferroelectrics, and Frequency Control **70**(7), 613–624 (Jul 2023)
21. Ye, T., Phan-Thien, N., Lim, C.T., Li, Y.: Red blood cell motion and deformation in a curved microvessel. Journal of Biomechanics **65**, 12–22 (Dec 2017)
22. Yiu, B.Y.S., Yu, A.C.H.: Least-squares multi-angle doppler estimators for plane-wave vector flow imaging. IEEE Transactions on Ultrasonics, Ferroelectrics, and Frequency Control **63**(11), 1733–1744 (Nov 2016)
23. Yiu, B.Y., Lai, S.S., Yu, A.C.: Vector projectile imaging: Time-resolved dynamic visualization of complex flow patterns. Ultrasound in Medicine & Biology **40**(9), 2295–2309 (Sep 2014)